GEOPHYSICS, VOL. 84, NO. 6 (NOVEMBER-DECEMBER 2019); P. 1–12, 22 FIGS., 4 TABLES.
10.1190/GEO2019-0031.1

Estimation of porosity and fluid saturation in carbonates from rock-physics templates based on seismic *Q*

Mengqiang Pang[1], Jing Ba[1], José M. Carcione[2], Stefano Picotti[3], Jian Zhou[1], and Ren Jiang[4]

ABSTRACT

Rock-physics templates establish a link between seismic properties (e.g., velocity, density, impedance, and attenuation) and reservoir properties such as porosity, fluid saturation, permeability, and clay content. We focus on templates based on attenuation (seismic Q or quality factor), which are highly affected by those properties, and we consider carbonate reservoirs that constitute 60% of the world oil reserves and a potential for additional gas reserves. The seismic properties are described with mesoscopic-loss models, such as the White model of patchy saturation and the double double-porosity model, which include frame and fluid heterogeneities. We have performed ultrasonic experiments, and we estimate the attenuation of the samples and the reservoir by using the spectral ratio method and the improved frequency-shift method. Then, multiscale calibrations of the templates are performed by using laboratory, well log, and seismic data. On this basis, reservoir porosity and fluid saturation are quantitatively evaluated. We first apply the templates to ultrasonic data of limestone using the White model. Then, we consider seismic data of a carbonate gas reservoir of MX work area in the Sichuan Basin, southwest China. A survey line in the area is selected to detect the reservoir by using the templates. The results indicate that the estimated porosity and saturation are consistent with well-log data and actual gas production results. The methodology indicates that the microstructural characteristics of a high-quality reservoir can effectively be predicted using seismic Q.

INTRODUCTION

The production of carbonate reservoirs plays a significant role in oil and gas technology (Sayers, 2008; Cao et al., 2018). Carbonate rocks are highly heterogeneous due to the presence of cracks and caves (Xu and Payne, 2009; Mousavi et al., 2012), and this characteristic favors hydrocarbon production in low-porosity/low-permeability reservoirs. However, due to the strong heterogeneities, it is difficult to treat these reservoirs with simple petrophysical models and processing techniques (Zhang et al., 2018).

Experimental studies and theories show that complex pores and cracks and heterogeneous saturation are responsible for the dispersion and attenuation of seismic waves (Dvorkin et al., 1994, 1995; Pride and Berryman, 2003a, 2003b; Gurevich et al., 2009; Ba et al., 2011; Tillotson et al., 2014; Mikhaltsevitch et al., 2016; Wang et al., 2016, 2017; Ding et al., 2018). White (1975) shows that attenuation and velocity dispersion measurements can be explained by the combined effect of mesoscopic-scale inhomogeneities and energy transfer between wave modes, with P-wave to slow P (Biot)-mode conversion being the main physical mechanism. We refer to this mechanism as mesoscopic loss (White, 1975; Dutta and Odé, 1979; Dutta and Seriff, 1979; Pride et al., 2004; Carcione and Picotti, 2006; Quintal, 2012). The mesoscopic-scale length is intended to be much larger than the grain sizes but much smaller than the wavelength of the pulse. Ba et al. (2013) use the Biot-Rayleigh equations, to describe seismic propagation in a double porosity medium, and make predictions in carbonate gas reservoirs. Based on the Biot-Rayleigh equations, Zhang et al. (2017) propose wave-propagation equations of a triple-porosity structure in conglomerates, which describe the effect of three types of pore shapes on

Manuscript received by the Editor 15 January 2019; revised manuscript received 17 April 2019; published ahead of production 30 July 2019.
[1]Hohai University, School of Earth Sciences and Engineering, Nanjing, China. E-mail: pmq@hhu.edu.cn; jba@hhu.edu.cn (corresponding author: Jing Ba); j_zhou@yahoo.com.
[2]Istituto Nazionale di Oceanografia e di Geofisica Sperimentale (OGS), Borgo Grotta Gigante 42c, Sgonico 34010, Trieste, Italy and Hohai University, School of Earth Sciences and Engineering, Nanjing, China. E-mail: jcarcione@inogs.it.
[3]Istituto Nazionale di Oceanografia e di Geofisica Sperimentale (OGS), Borgo Grotta Gigante 42c, Sgonico 34010, Trieste, Italy. E-mail: spicotti@inogs.it.
[4]China Petroleum Exploration and Development Research Institute, Langfang Branch, Langfang 065000, China. E-mail: jiangr69@petrochina.com.cn.

the seismic waves. The mesoscopic mechanism or wave-induced local fluid flow is considered to be one of the most significant wave-loss mechanisms (Carcione, 2014; Ba et al., 2016; Spencer and Shine, 2016; Guo et al., 2018c). Recently, researchers proposed several models to consider the heterogeneity of rock internal structure and fluid saturation (Kong et al., 2013, 2017; Amalokwu et al., 2017; Guo et al., 2018a, 2018b; Qin et al., 2018a, 2018b). Ba et al. (2017) propose a double double-porosity (DDP) structure theory, which considers the complex situation of the double-pore structure and patchy saturation in the same model.

Based on sensitivity analyses of reservoir properties, P-wave attenuation is very sensitive to the fluid type and content and P-wave impedance is a good indicator of porosity (Guo et al., 2015; Zeng et al., 2017; Ba et al., 2018; Picotti et al., 2018). Seismic wave attenuation can be a direct hydrocarbon indicator (Quan and Harris, 1997; Liu and Sun, 2009). Ba et al. (2018) analyze the attenuation characteristics of 10 carbonate samples and verify that P-wave attenuation can be used as an effective indicator for characterizing reservoirs. Cao et al. (2018) analyze carbonate reservoirs in the south part of the Tarim Basin and find that Q and velocity dispersion are closely related to the fracture density and the fluid type.

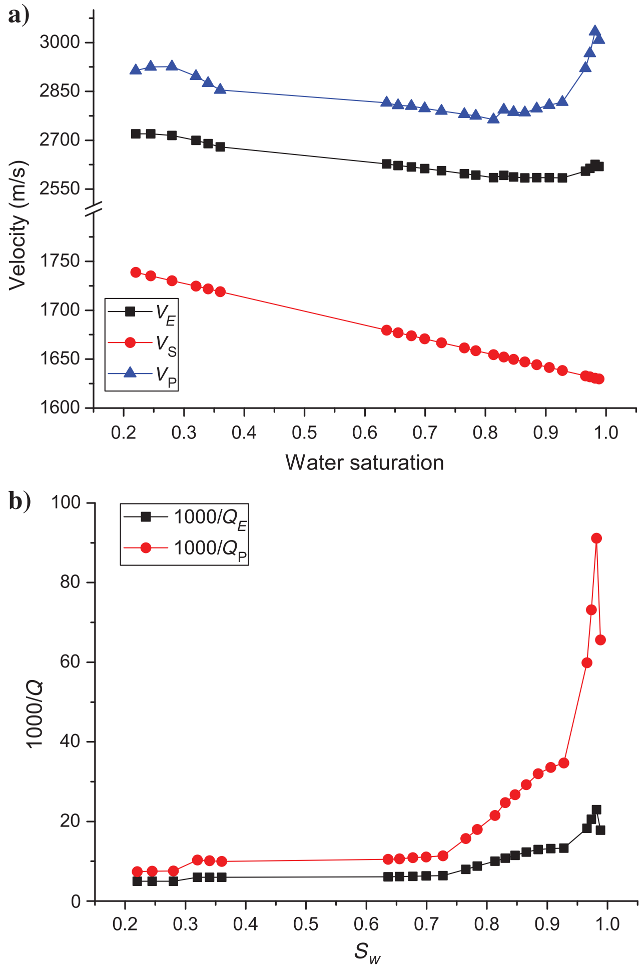

Figure 1. (a) Velocities and (b) dissipation factors as a function of water saturation.

Rock-physics templates (RPTs) can link the seismic properties to the reservoir characteristics (e.g., Carcione and Avseth, 2015). Dvorkin and Mavko (2006) first present an attenuation-based template and Picotti et al. (2018) extend this work to establish a complete set of RPTs based on seismic Q and study the effects of fluid saturation, porosity, and permeability. They use a generalization of the Johnson mesoscopic-loss model (Johnson, 2001) in the case of fractal gas patches with a distribution of sizes in water- and oil-saturated rocks. The Johnson model describes seismic velocity and Q for gas patches of varying shapes, other than the spherical one (White model). Here, we select P-wave Q and impedance to build the RPTs. To relate reservoir porosity and saturation with the seismic response, ultrasonic, well, and seismic data are used to calibrate the templates. Then, by superposing the seismic properties on the templates, a quantitative interpretation of the reservoir porosity and gas saturation can be performed.

WHITE MODEL: ULTRASONIC DATA OF LIMESTONES

We consider the data in Figures 2 and 4 of Cadoret et al. (1995) (velocity versus water saturation) and Figure 1 of Cadoret et al. (1998) (Q factor versus water saturation). The rock is Estaillades Limestone, the frequency is 1 kHz (sonic band), the porosity is 0.3, the permeability is 255 mdarcy, and the experiment is a drying one, in which gas (CO_2) patches are created. The experiment is performed at atmospheric pressure in resonant bars. The data are given as extensional-wave velocity V_E, S-wave velocity V_S, and extensional-wave quality factor Q_E. To obtain the P-wave values (V_P and Q_P), we use the following equations (Cadoret et al., 1995):

$$V_P^2 = \frac{V_S^2(4V_S^2 - V_E^2)}{3V_S^2 - V_E^2}, \tag{1}$$

(to use for Poisson's ratios, $\nu < 0.4$; here the range is 0.22–0.29), and (Mavko et al., 2009)

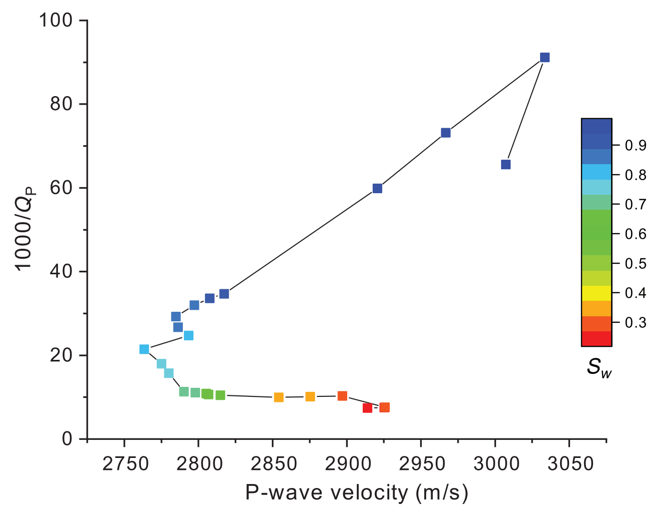

Figure 2. The P-wave velocity as a function of the dissipation factor.

$$
\begin{aligned}
\frac{(1-\nu)(1-2\nu)}{Q_{\mathrm{P}}} &= \frac{(1+\nu)}{Q_E} - \frac{2\nu(2-\nu)}{Q_{\mathrm{S}}}, \\
\nu &= \frac{(V_{\mathrm{P}}/V_{\mathrm{S}})^2 - 2}{2[(V_{\mathrm{P}}/V_{\mathrm{S}})^2 - 1]},
\end{aligned} \tag{2}
$$

where we assume $Q_{\mathrm{S}} = 270$ at all saturations (see ~~Figure 3 of~~ Cadoret et al., 1998). For S-waves, the experimental results show little variation of the velocity with frequency. The variation of the S-wave velocity with saturation in Cadoret et al. (1995) is explained by the density effect, so there is practically no velocity dispersion and the attenuation is very weak. Table 1 gives the values of the different properties, and the data are represented in Figure 1. The saturations correspond to the experimental points of the extensional velocities V_E. The quality factors Q_E have been linearly interpolated to these points. Figure 2 shows the dissipation factor as a function of the P-wave velocity to be used in the template.

Table 2 shows the properties to fit the data using the Biot-White model (White, 1975; Carcione, 2014). Microstructural data about the Estaillades Limestone can be found in Rasolofosaon and Zinszner (2007), where the dry-rock bulk and shear moduli are estimated as $K_m = 12.3$ GPa and $\mu_m = 6$ GPa, respectively, using the phase

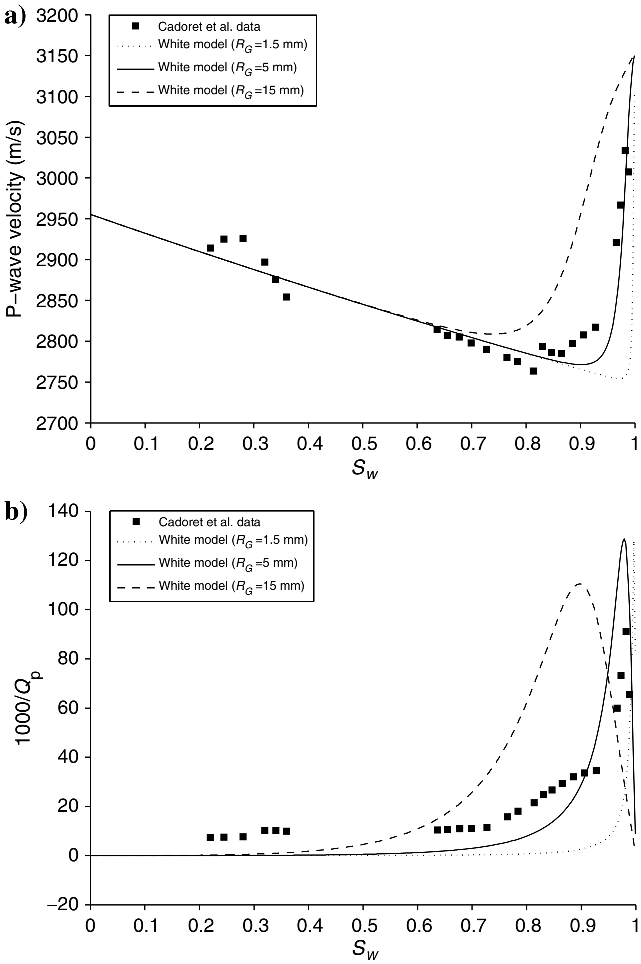

Figure 3. (a) The P-wave velocity and (b) dissipation factor as a function of water saturation. Fit with the White mesoscopic model. The term R_G is the radius of the gas patches.

technique, whereas the grain bulk modulus is $K_s = 79$ GPa. However, the samples used by Cadoret et al. (1995, 1998) were not the same because the reported permeability is 180 mdarcy in Rasolofosaon and Zinszner (2007). Cadoret et al.'s (1995, 1998)

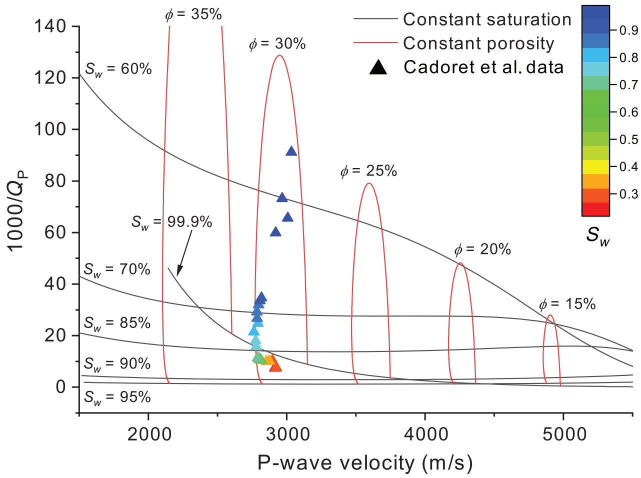

Figure 4. The RPT for the Estaillades Limestone.

Table 1. Experimental properties of the Estaillades Limestone.

S_w	V_E	V_{S} (m/s)	$1000/Q_E$	V_{P} (m/s)	$1000/Q_{\mathrm{P}}$
0.220	2720	1739	5	2914	7.4
0.245	2720	1735	5	2925	7.5
0.280	2715	1730	5	2926	7.6
0.320	2700	1725	6	2897	10.3
0.340	2690	1722	6	2875	10.1
0.360	2680	1719	6	2854	10
0.636	2627	1680	6.1	2815	10.5
0.655	2622	1677	6.1	2807	10.6
0.677	2618	1674	6.2	2805	10.9
0.699	2613	1671	6.3	2798	11.1
0.727	2606	1667	6.4	2790	11.3
0.765	2598	1661	7.9	2780	15.7
0.784	2593	1659	8.8	2775	18
0.813	2585	1654	10	2763	21.5
0.830	2592	1652	10.8	2793	24.7
0.847	2588	1650	11.5	2786	26.7
0.865	2584	1647	12.3	2785	29.2
0.885	2585	1644	12.9	2797	32.2
0.906	2585	1641	13.2	2808	33.6
0.927	2585	1638	13.3	2817	34.7
0.966	2605	1633	18.3	2921	58.9
0.973	2614	1632	20.5	2967	73.2
0.982	2626	1631	23	3033	91.2
0.988	2620	1630	17.8	3007	65.6

Note: $Q_{\mathrm{S}} = 270$, $\phi = 0.3$, and $\kappa = 255$ mdarcy.

samples have a permeability of 255 mdarcy and possibly a slightly weaker frame (smaller frame moduli) as shown in Table 2.

We use the Krief model to obtain the dry-rock moduli K_m and μ_m. The moduli are given by

$$K_m = K_s(1-\phi)^{A/(1-\phi)},$$
$$\mu_m = K_m\mu_s/K_s, \tag{3}$$

Table 2. Biot properties of the Estaillades Limestone.

Grain bulk modulus K_s	77 GPa
Shear modulus μ_s	32 GPa
Density ρ_s	2710 $\mathrm{kg/m^3}$
Frame bulk modulus K_m	10.66 GPa
Shear modulus μ_m	4.43 GPa
Porosity ϕ	0.3
Permeability κ	0.255 darcy
Water density ρ_w	1000 $\mathrm{kg/m^3}$
Viscosity η_w	0.0012 Pa s
Bulk modulus K_w	2.25 GPa
Gas density ρ_g	1.6 $\mathrm{kg/m^3}$
Viscosity η_g	0.000016 Pa s
Bulk modulus K_g	0.125 MPa

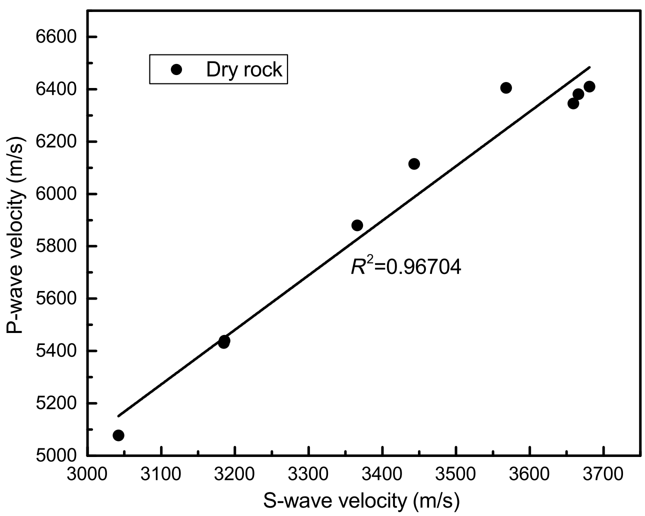

Figure 5. Crossplot of the P- and S-wave velocities, where R^2 is the goodness of fit.

Table 3. Properties of the carbonate samples.

Samples	A	B	C	D	E	F	G	H	I
Porosity (%)	16.87	11.75	11.63	6.93	6.08	5.47	5.34	5.10	4.99
Permeability (mdarcy)	3.31	0.075	0.138	0.601	0.13	0.174	0.458	0.091	1.34
Dry-rock density ($\mathrm{g/cm^3}$)	2.32	2.45	2.45	2.64	2.65	2.67	2.66	2.69	2.67

where K_s and μ_s are the bulk modulus and shear modulus of the rock matrix, respectively, ϕ is the porosity, and $A = 3.88$ for this data set (see Table 1). Permeability is related to porosity by the Kozeny-Carman relation (Mavko et al., 2009):

$$\kappa = \frac{\kappa_0\phi^3}{(1-\phi)^2}, \tag{4}$$

where $\kappa_0 = 4628$ mdarcy gives $\kappa = 255$ mdarcy.

A detailed procedure to obtain the wave velocity and Q for White model can be found in Carcione et al. (2012). Figure 3 compares the theoretical and experimental results, in which the optimal radius of the gas patches is 5 mm, with White model capturing the attenuation peak at high water saturations. The template is shown in Figure 4. As can be appreciated, it allows us to determine porosity and saturation.

DDP MODEL: A CARBONATE RESERVOIR

The research area is the carbonate gas reservoir of the MX work area in the Sichuan Basin, southwest China. The ultrasonic P- and S-wave measurements were performed on cores of nine carbonate rocks. The samples are cylinders 25.2 mm in diameter and 30–42 mm in length. The experiments were performed at a confining pressure of 80 MPa, a temperature of 20°C, and a pore pressure of 10 MPa. The ultrasonic testing was performed using the experimental setup of Guo et al. (2009), and the procedure of Ba et al. (2016) is adopted to measure the ultrasonic waveforms at partial-saturation (gas-water) conditions. A fully water-saturated sample was dried in an oven to vary the saturation, which was controlled according to the sample weight. Then, a fixed confining pressure was exerted to the samples, gas was injected at a given pore pressure, and the waveforms were recorded. The quality factor Q can be determined by the spectral ratio method using a reference standard material with a very high (&in$f$in;) quality factor (Toksöz et al., 1979; Guo and Fu, 2006; Picotti and Carcione, 2006), from

$$\ln\left[\frac{A_1(f)}{A_2(f)}\right] = -\frac{\pi x f}{QV} + \ln\left[\frac{G_1(f)}{G_2(f)}\right], \tag{5}$$

where f is the frequency, A_1 and A_2 are the amplitude spectra of the rock and the standard material, respectively, x is the traveling distance, V is the wave velocity, and G_1 and G_2 denote the geometric spreading in the rock and standard material, respectively.

On the other hand, the attenuation dependence on saturation is estimated by using the measurement at full-gas saturation as a reference. In this case,

$$\ln\left[\frac{A_1(f)}{A_2(f)}\right] = -\frac{\pi x f}{Q_r V} + \ln\left[\frac{G_1(f)}{G_2(f)}\right] = \pi x f\left(\frac{1}{Q_g V_g} - \frac{1}{QV}\right) + \ln\left[\frac{G_1(f)}{G_2(f)}\right] \tag{6}$$

and

$$\frac{1}{Q_r} = \frac{1}{Q} - \frac{V}{V_g Q_g}, \tag{7}$$

where V_g and Q_g are the quantities at full gas saturation.

To estimate the P-wave attenuation, we analyze the waveforms after the first arrival of the P-wave. Then, the spectra of the corresponding waveforms are obtained with the fast Fourier transform and selecting the appropriate frequency band. We calculate the spectral ratio using least squares to fit the main frequency band. The experimental properties of the nine carbonate samples are given in Tables 3 and 4, and the attenuation of the samples is calculated using equations 5 and 6. Figures 5 and 6 show the crossplot of the P- and S-wave velocities and the variation of the velocity and attenuation with water saturation, respectively. Figure 6a indicates that the P-wave velocity increases with increasing water saturation. Attenuation shows a tendency to increase first and then decrease as the water saturation increases (Figure 6b).

Estimation of attenuation

The lithology of the reservoir rocks in this area includes residual granule and crystalline dolomites. The major reservoir space is composed of vugs and residual intergranular and intercrystalline pores. The reservoir is characterized as "fractured vugs" and "fractured pores" types with an average porosity of 4.24% and a thickness of approximately 36 m. There is a large area of grain shoal facie generation, which lays out the conditions for a good reservoir.

Quan and Harris (1997) propose a centroid-frequency-shift method to estimate the quality factor, assuming that the amplitude spectrum satisfies a Gaussian distribution. As a statistical feature, use of the centroid shift can effectively improve the stability of Q estimation. However, there are some drawbacks because the shape of the spectrum may differ from a Gaussian function. Zhang and Ulrych (2002) propose a frequency-shift analysis based on the peak frequency, assuming a Ricker wavelet. The method is more reasonable for practical applications, and the results are accurate. However, insufficient stability is always a major problem due to the presence of noise.

To reduce the limitations of the two methods, researchers (Tu and Lu, 2009; Hu et al., 2013; Li et al., 2015) proposed an improved frequency-shift method. The main idea of the method is to derive the quality factor from the centroid frequency of the amplitude spectrum as

$$Q = \frac{\sqrt{\pi^5} t f_1 f_0^2}{16(f_0^2 - f_1^2)}, \tag{8}$$

where t is the propagation time and f_0 and f_1 are the centroid frequencies of the signal before and after propagation, respectively. This equation combines the advantages of the two types of frequency-shift methods, with better stability and higher accuracy. We select the strong reflection layer covering the target as the reference. Due to the strong stability of the centroid, we select the main frequency band to estimate the attenuation. Figure 7a shows an example of seismic data, in which the red points are the waveform data of the target layer, and Figure 7b shows the time-frequency map of the seismic trace. Figure 7c shows the spectra to compute attenuation from equation 8. Figure 8 displays the amplitude and the computed attenuation (the dissipation factor $1000/Q$), where MX8, MX17, and MX204 are three wells. The results show that there is a strong attenuation anomaly around these wells. Areas with high attenuation have a large lateral distribution and good continuity.

Table 4. Experimental properties of the carbonate samples.

Samples	S_w (%)	V_P (m/s)	$1000/Q_r$	Samples	S_w (%)	V_P (m/s)	$1000/Q_r$
A	0	5099	0	F	0	6410	0
	12	5078	3.9		14	6412	1
	23	5168	17.9		26	6412	1.8
	36	5176	19.7		40	6418	2.4
	51	5223	24.3		53	6428	3.6
	64	5240	26.4		67	6452	5
	77	5262	20		79	6458	6.2
	88	5299	22		89	6484	8
	100	5375	26.4		100	6547	6
B	0	5440	0	G	0	6382	0
	12	5444	2		13	6382	0.4
	26	5447	3.5		27	6388	1
	39	5464	4.7		39	6407	1.2
	51	5483	6.1		55	6399	1.6
	64	5493	8.5		66	6422	2
	77	5513	9.1		75	6445	4
	89	5538	11.1		85	6461	6.2
	100	5624	7.5		100	6517	4.7
C	0	5431	0	H	0	6346	0
	10	5437	1.7		13	6363	0.2
	21	5443	5.1		30	6372	1.6
	35	5458	4.6		41	6380	0.9
	48	5474	6.5		52	6397	1.7
	61	5488	13.2		63	6407	2.2
	74	5500	7.7		78	6424	5.5
	86	5521	6.9		87	6432	7.4
	100	5620	4.4		100	6485	9.4
D	0	5880	0	I	0	6406	0
	13	5860	2.8		13	6443	5.1
	26	5921	2.3		27	6406	2
	38	5890	1.4		41	6462	4.4
	51	5931	1.2		54	6462	6.3
	64	5921	2.9		67	6490	7.3
	77	6003	3.7		77	6500	5.9
	88	5972	1.5		88	6529	3.9
	100	6025	2.2		100	6529	8.4
E	0	6115	0				
	12	6098	1.2				
	26	6131	2.6				
	40	6173	2.3				
	55	6102	2.8				
	68	6119	4.6				
	79	6123	5.5				
	89	6165	4.2				
	100	6199	5.4				

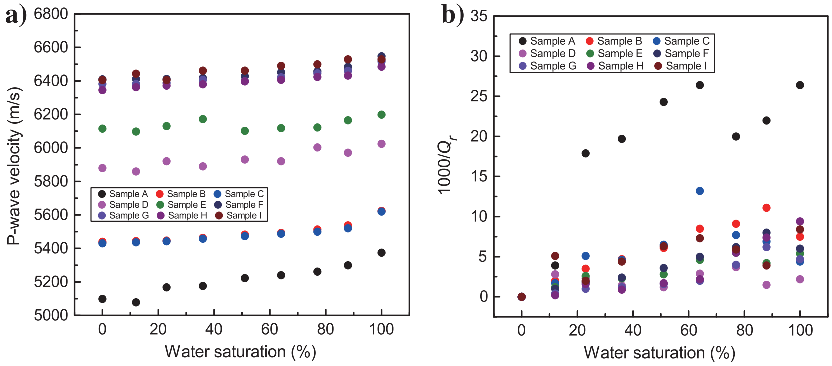

Figure 6. Variation of the (a) velocity and (b) attenuation with water saturation.

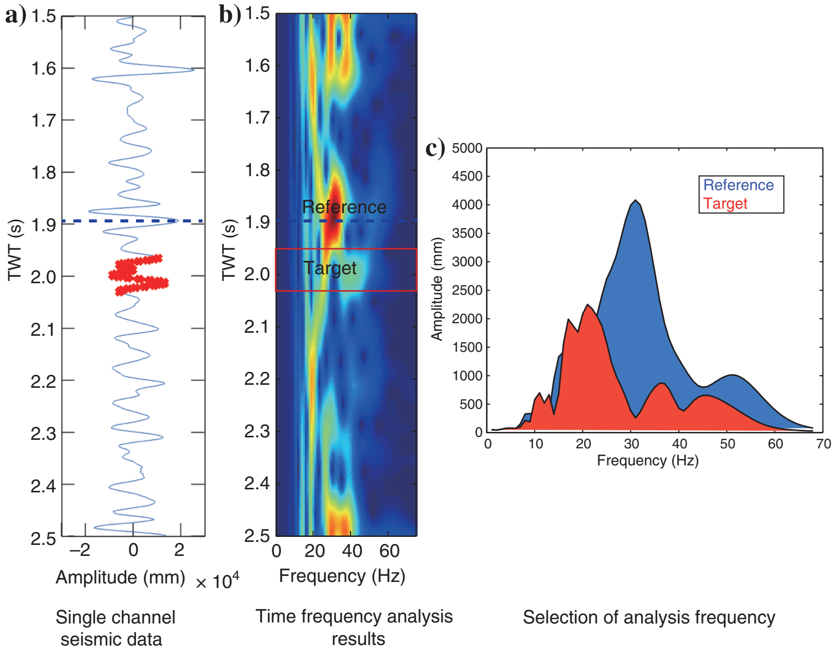

Figure 7. Procedure for the improved frequency-shift method.

Rock-physics behavior

The velocity Q model

The DDP model considers an inclusion with different porosity, permeability, and compressibility characteristics embedded in a host medium. The mineral composition of the inclusion and the host medium is the same. This model also considers patchy saturation in the host, and the fluid in the inclusion is mainly water. The time-domain dynamical equations were derived from the Hamilton principle. The theory is based on the Biot-Rayleigh model and the dynamical equations can be found in Ba et al. (2017). A double Fourier transform of these equations to the real frequency (ω)-complex wavenumber (k) domain yield the phase velocity and quality factor,

$$V = \left[\mathrm{Re}\left(\frac{1}{V_c}\right)\right]^{-1} \tag{9}$$

and

$$Q = \frac{\mathrm{Re}(V_c^2)}{\mathrm{Im}(V_c^2)}, \tag{10}$$

where $V_c = \omega/k$ is the complex velocity of the fast P-wave.

Effects of frame and fluid heterogeneities

The immiscible fluids (gas and water) are unevenly distributed in pores and cracks. According to geologic data, logging interpretation, and experiment observations, the carbonate minerals are mainly dolomite with a small amount of clay. The pore space is mainly composed of intergranular pores and cracks (see Figure 9). Consider sample A in Table 3 as a reference, with an inclusion

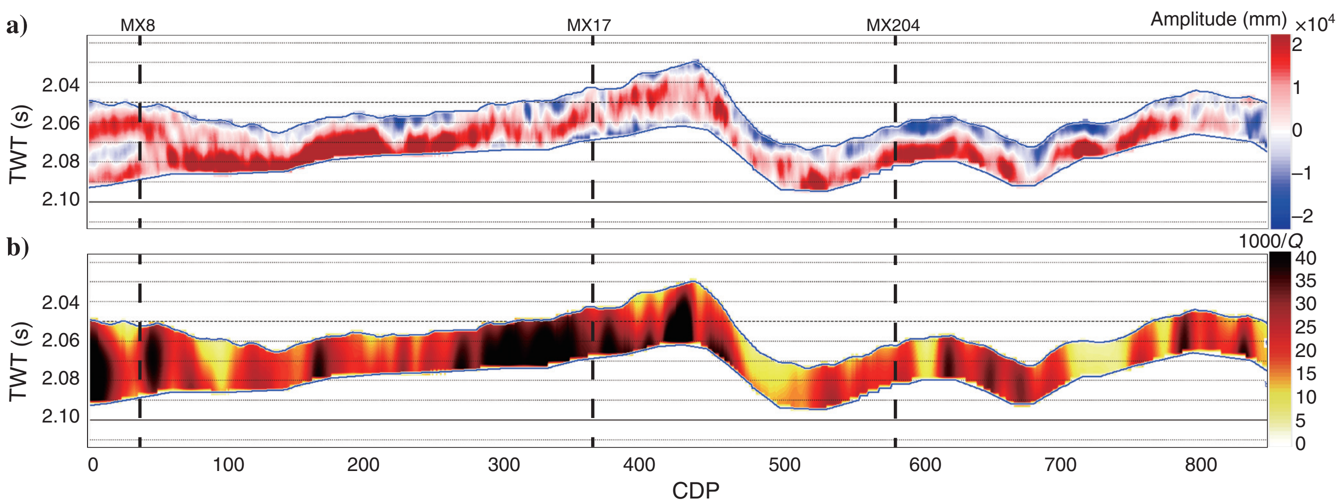

Figure 8. Reservoir seismic (a) amplitude and (b) attenuation.

radius of 50 µm. We assume the following fluid parameters: water: bulk modulus = 2.24 GPa, density = 1.0016 g/cm^3, and viscosity = 0.00098 Pa s; gas: bulk modulus = 0.017 GPa, density = 0.089 g/cm^3, viscosity = 0.000016 Pa s, and gas pocket radius = 80 µm. The stiffnesses moduli of the dry rocks are obtained from the P- and S-wave velocities using the Gassmann equations (e.g., Carcione, 2014). Permeability is related to porosity in equation 4. By adjusting the volumetric percentage of the inclusions and the saturation of the fluids, we can describe the effects of the heterogeneities on P-wave attenuation and velocity dispersion.

The calculations assume 100% gas, 100% water, and 87% water saturation. The volumetric percentages of the inclusions are 0.0002, 0.002, 0.02, and 0.1. Figures 10, 11, and 12 show the P-wave dispersion and attenuation for the three saturation states, and the frequency range is 10^4–10^8 Hz. In all of the cases, the P-wave dispersion gradually increases with the volume ratio of the inclusions and the corresponding attenuation increases accordingly. When the volume ratio of the inclusions is small, the relaxation peaks caused by the frame and fluid heterogeneities unevenly overlap, whereas the peaks tend to separate when the volume ratio gradually increases. As the water saturation increases, dispersion and attenuation increase first and then decrease.

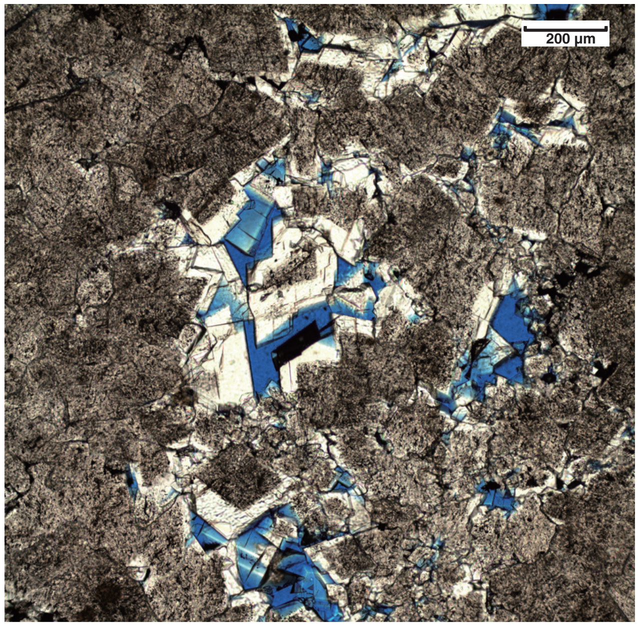

Figure 9. Scanning electron microscopy of a carbonate rock (the white is dolomite, the black is pitch, the brown is feldspar, and the blue is water).

Effect of fluid saturation

Water saturation varies from 0 to 100%, and the frequency range is 10^4–10^7 Hz. Figure 13 shows the dispersion and attenuation of the P-wave as a function of frequency. Dispersion and attenuation increase first and then decrease with water saturation. At full water saturation, the loss due to frame heterogeneity dominates.

Figure 14 shows the dispersion and attenuation of the P-wave at different water saturations, at the frequency range of 10–1000 Hz. The radius of the inclusion and the gas pocket is assumed to be 80 and 50 mm, respectively. Contrary to the ultrasonic case, dispersion and attenuation decrease smoothly when approaching full water saturation. Because the gas viscosity is much smaller than that of water, attenuation and dispersion induced by fluid flow at high frequencies is dominated by gas mobility, whereas water effects prevail at low frequencies.

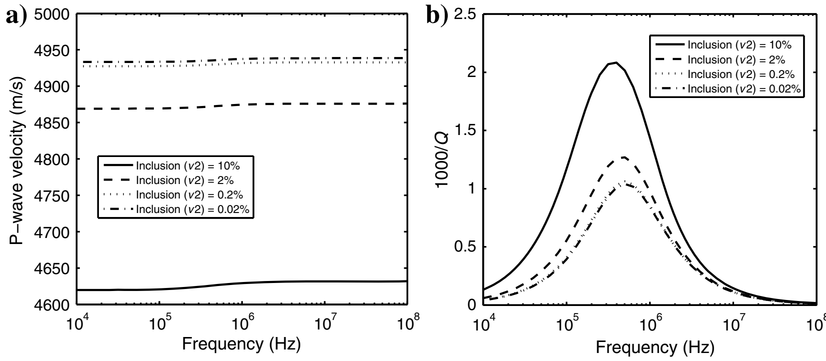

Figure 10. Effects of the volumetric percentage of the inclusions on (a) velocity dispersion and (b) attenuation at full gas saturation.

Calibration of the RPTs

The carbonates are mainly composed of dolomite. According to Mavko et al. (2009), the bulk modulus of dolomite is 94.9 GPa, and its the shear modulus is 45 GPa. The average Voigt-Reuss-Hill equation (Voigt, 1910; Reuss, 1929; Hill, 1952; Picotti et al., 2018) is used to estimate the elastic parameters and density of the rock frame. The differential effective medium model is used to calculate the bulk and shear modulus of the rock frame and inclusion (Kumar and Han, 2005; Baechle et al., 2008; Sun et al., 2012). The bulk modulus and density of water and natural gas at reservoir pressure-temperature conditions are obtained from Batzle and Wang (1992).

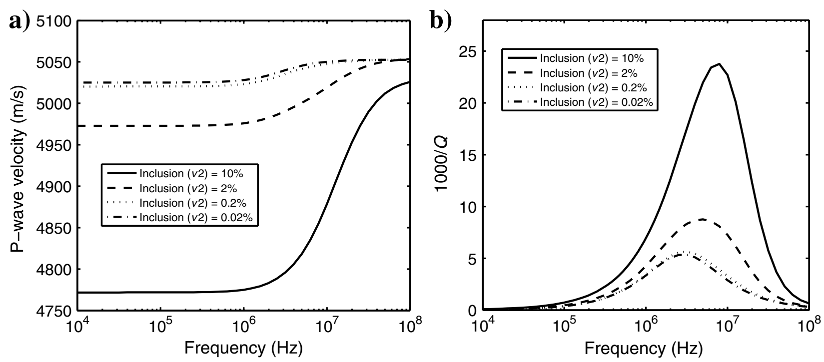

Figure 11. Effects of the volumetric percentage of the inclusions on (a) velocity dispersion and (b) attenuation at full water saturation.

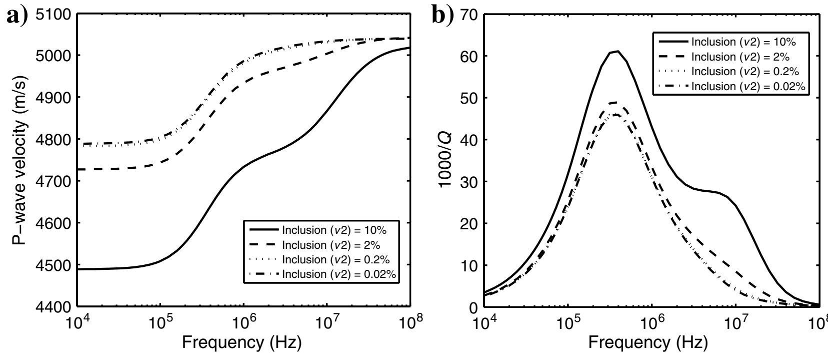

Figure 12. Effects of the volumetric percentage of the inclusions on (a) velocity dispersion and (b) attenuation at 87% water saturation.

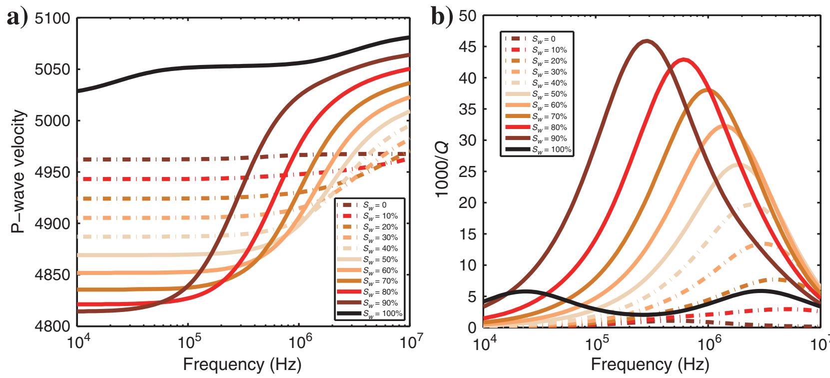

Figure 13. Effect of water saturation on (a) velocity dispersion and (b) attenuation at ultrasonic frequencies.

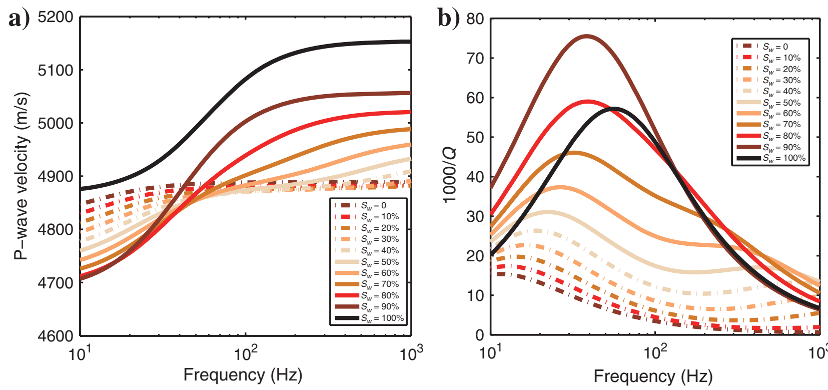

Figure 14. Effect of water saturation on (a) velocity dispersion and (b) attenuation at seismic frequencies.

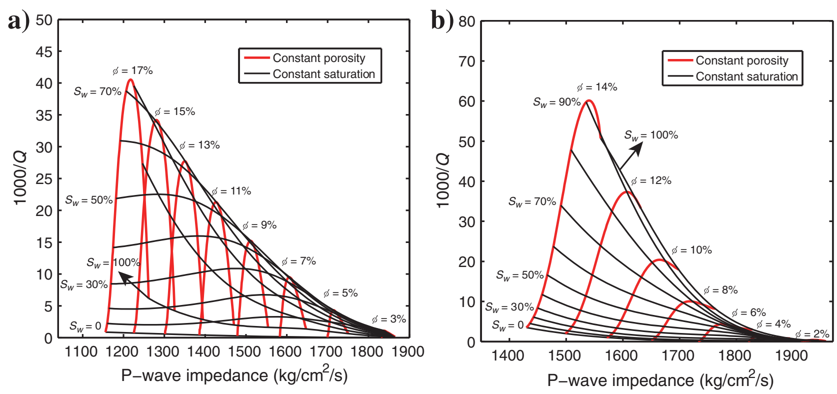

Figure 15. The RPTs at (a) ultrasonic and (b) seismic frequencies.

Figure 15 shows the templates at ultrasonic (1 MHz) and seismic (50 Hz) frequencies. The grain bulk and shear moduli are 88 and 56 GPa, respectively, and the frame bulk and shear moduli range is 25–63 and 16–43 GPa, respectively. The fluid parameters are the same as above. The inclusion and gas pocket radii are 80 and 50 μm at ultrasonic frequencies and 80 and 50 mm at seismic frequencies, respectively. The volumetric percentage of the inclusions is 0.002. The curves correspond to isolines of constant saturation and constant porosity. Attenuation decreases for increasing impedance with increasing porosity at a fixed saturation. At constant porosity, attenuation increases and then decreases.

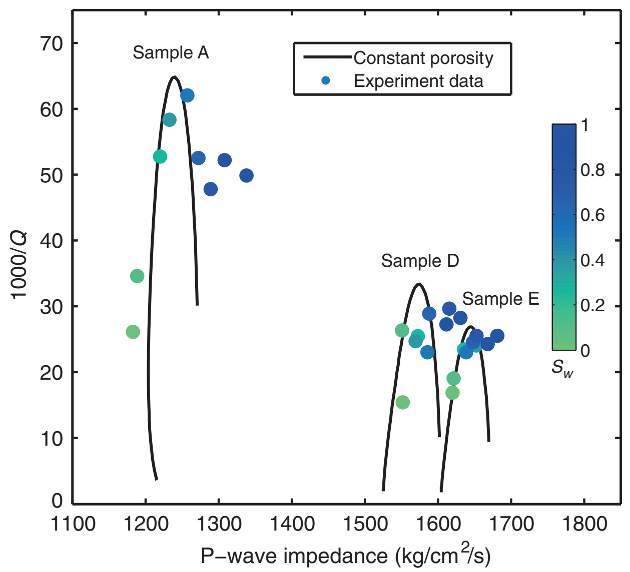

Figure 16. Attenuation versus P-wave impedance for three carbonate samples and curves prediction by the ~~Biot-Rayleigh~~ DDP model.

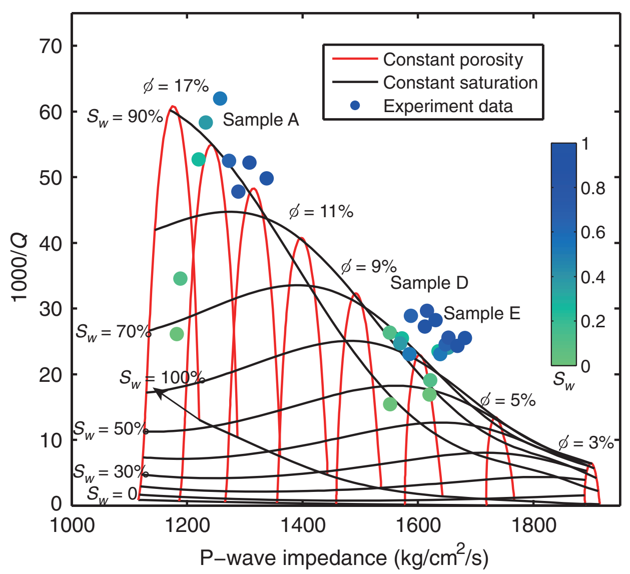

Figure 17. The RPT. Ultrasonic frequency.

Calibration at ultrasonic frequencies

First, it is necessary to calibrate the templates. Figure 16 shows the calibration for samples A, D, and E in Table 3, and Figure 17 shows the complete prediction template. The sample porosity is well-matched, but the agreement is not so good when the water saturation varies. For increasing water saturation, the trends agree. Based on the measurements at full gas saturation as a reference, we use equation 6 to calculate the attenuation dependence on saturation for each sample. Correspondingly, the relative Q factor replaces the P-wave one to obtain the RPT, which is compared with the corresponding sample features (see Figure 18). Each dot is color coded by the relative attenuation value; the sample numbers are A-I from left to right (see Table 3). The agreement is good for the porosity and the water saturation.

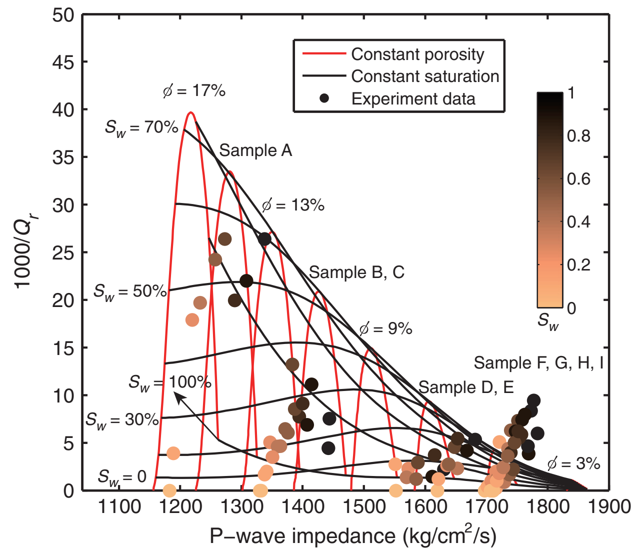

Figure 18. The RPT (Q^r). Ultrasonic frequency.

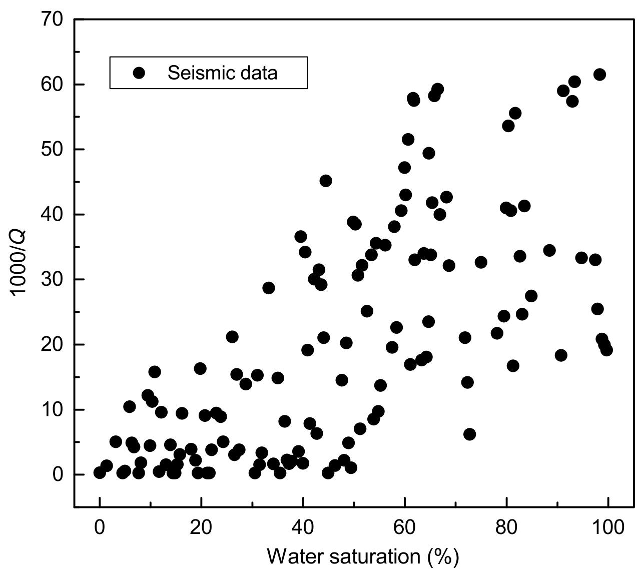

Figure 19. Relationship between the attenuation of seismic data and the water saturation.

Calibration at seismic frequencies

Attenuation is obtained using the improved frequency-shift method (equation 8), and the P-wave impedance is obtained from the inversion of seismic data. Here, we use the well-log porosity and saturation. As shown in Figure 19, attenuation generally increases with increasing water saturation. Figure 20 shows the projection of the data on the template; water saturation is color coded. Attenuation increases gradually with increasing water saturation, which is consistent with the data. The average porosity gradually decreases from left to right, and this trend is well-matched by the template.

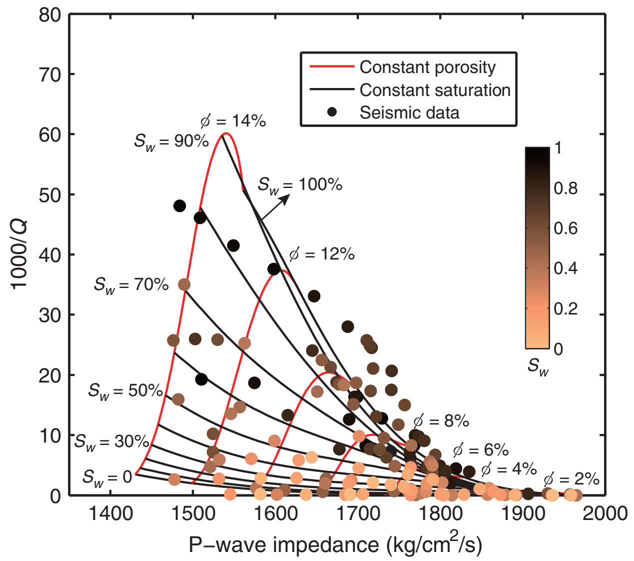

Figure 20. The RPT. Seismic frequency.

Porosity and saturation estimation

The quantitative estimation of porosity and gas saturation is carried out for three wells, namely, MX8–MX17–MX204 (see Figures 21 and 22). The porosity range is approximately 2%–12%, with wells MX8 and MX204 showing higher gas content, whereas well MX17 reveals the presence of water. The inverted profiles indicate an upper gas layer and a lower water layer, which is consistent with the type of geologic structure. High gas content correlates with high porosity (see the inversion results in Figure 22a and 22b). From log interpretation and gas production results, the effective reservoir porosity of wells MX8 and MX204 is 4%–9%, and these are high-production gas wells, with 1.9068 and 1.1562 million cubic meters per day, respectively. The gas production of well MX17 is relatively lower, with 0.532 million cubic meters per day. The inversion results agree with the actual gas production and saturation profiles. The porosity range of the logs is well-matched. Moreover, the method can be used to estimate the porosity and saturation of the whole 3D area. In general, the RPTs based on seismic attenuation can satisfactorily be applied to carbonate-reservoir prediction and fluid quantitative interpretation.

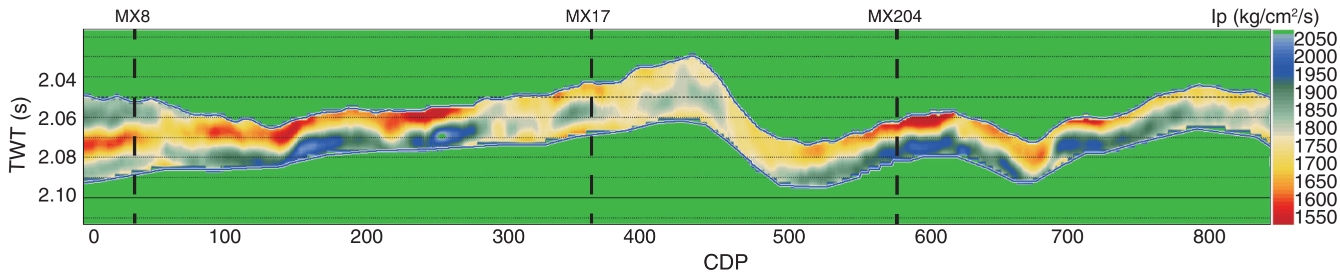

Figure 21. The P-wave attenuation and impedance profiles.

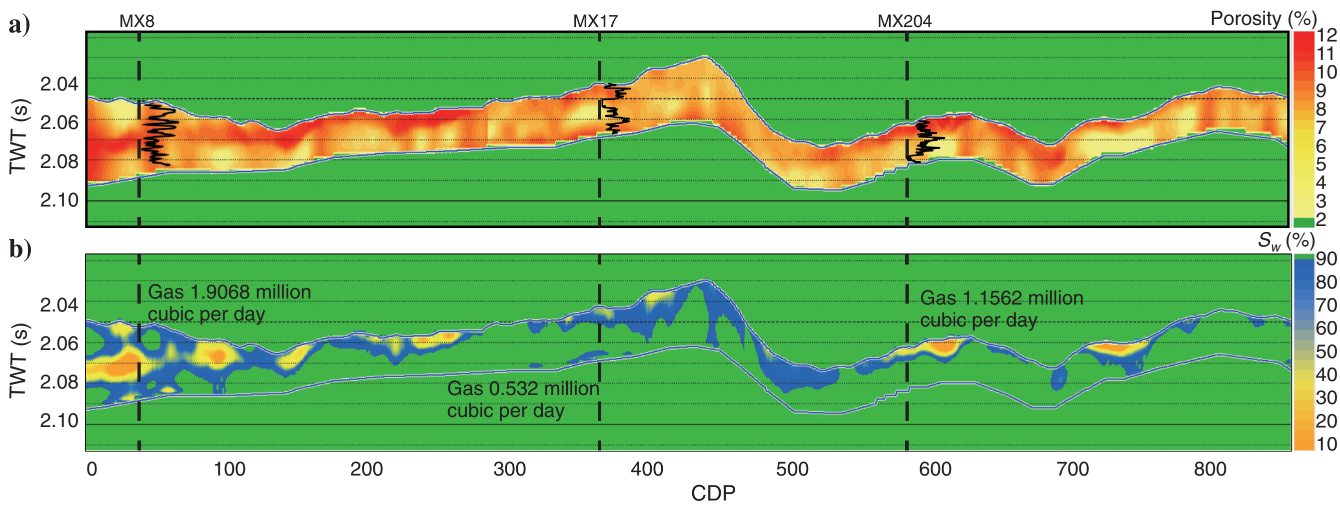

Figure 22. (a) Porosity and (b) saturation profiles.

CONCLUSION

We propose a methodology to estimate porosity, saturation, and possibly permeability from seismic data, using RPTs based on the seismic attenuation of P-waves. The loss/dispersion model is the double-double porosity ~~Biot-Rayleigh~~ theory of wave-induced fluid-flow attenuation, and the approach is applied to carbonate rocks of the MX work area. Because P-wave attenuation and acoustic impedance are very sensitive to porosity and saturation, crossplots of these properties, which are obtained by inverting poststack data, are chosen to build the templates. The results are consistent with actual porosity and gas production in the reservoir. Thus, these templates can be conclusively used to predict reservoir fluid saturation and porosity based on seismic data.

ACKNOWLEDGMENTS

The authors are grateful to the support of the Cultivation Program of "111" Plan of China, Jiangsu Innovation and Entrepreneurship Plan, Specially-Appointed Professor Plan of Jiangsu Province, the Fundamental Research Funds for the Central Universities, China (grant no. 2016B13114), and the National Natural Science Foundation of China (grant no. 41974123, 41704109).

DATA AND MATERIALS AVAILABILITY

Data associated with this research are available and can be obtained by contacting the corresponding author.

REFERENCES

Amalokwu, K., G. Papageorgiou, M. Chapman, and A. I. Best, 2017, Modelling ultrasonic laboratory measurements of the saturation dependence of elastic modulus: New insights and implications for wave propagation mechanisms: International Journal of Greenhouse Gas Control, **59**, 148–159, doi: 10.1016/j.ijggc.2017.02.009.

Ba, J., J. M. Carcione, and J. Nie, 2011, Biot-Rayleigh theory of wave propagation in double-porosity media: Journal of Geophysical Research, **116**, B06202, doi: 10.1029/2010JB008185.

Ba, J., W. Xu, L.-Y. Fu, J. M. Carcione, and L. Zhang, 2017, Rock anelasticity due to patchy-saturation and fabric heterogeneity: A double double-porosity model of wave propagation: Journal of Geophysical Research: Solid Earth, **122**, 1949–1971, doi: 10.1002/2016JF004153.

Ba, J., X. F. Yan, Z. Y. Chen, G. C. Xu, and C. S. Bian, 2013, Rock physics model and gas saturation inversion for heterogeneous gas reservoirs (in Chinese): Chinese Journal of Geophysics, **56**, 1696–1706.

Ba, J., L. Zhang, and D. Wang, 2018, Experimental analysis on P-wave attenuation in carbonate rocks and reservoir identification: Journal of Seismic Exploration, **27**, 371–402.

Ba, J., J. Zhao, J. M. Carcione, and X. Huang, 2016, Compressional wave dispersion due to rock matrix stiffening by clay squirt flow: Geophysical Research Letters, **43**, 6186–6195, doi: 10.1002/2016GL069312.

Baechle, G. T., A. Colpaert, G. P. Eberli, and R. J. Weber, 2008, Effects of microporosity on sonic velocity in carbonate rocks: The Leading Edge, **27**, 1012–1018.

Batzle, M., and Z. J. Wang, 1992, Seismic properties of pore fluids: Geophysics, **57**, 1396–1408, doi: 10.1190/1.1443207.

Cadoret, T., D. Marion, and B. Zinszner, 1995, Influence of frequency and fluid distribution on elastic wave velocities in partially saturated limestones: Journal of Geophysical Research, **100**, 9789–9803, doi: 10.1029/95JB00757.

Cadoret, T., G. Mavko, and B. Zinszner, 1998, Fluid distribution effect on sonic attenuation in partially saturated limestones: Geophysics, **63**, 154–160, doi: 10.1190/1.1444308.

Cao, Z. N., X. Y. Li, J. Liu, X. Qin, S. Sun, Z. Li, and Z. Cao, 2018, Carbonate fractured gas reservoir prediction based on P-wave azimuthal anisotropy and dispersion: Journal of Geophysics and Engineering, **15**, 2139–2149, doi: 10.1088/1742-2140/aabe58.

Carcione, J. M., 2014, Wave fields in real media, Theory and numerical simulation of wave propagation in anisotropic, anelastic, porous and electromagnetic media, 3rd ed.: Elsevier (extended and revised), 65–121.

Carcione, J. M., and P. Avseth, 2015, Rock-physics templates for clay-rich source rocks: Geophysics, **80**, no. 5, D481–D500, doi: 10.1190/geo2014-0510.1.

Carcione, J. M., D. Gei, S. Picotti, and A. Michelini, 2012, Cross-hole electromagnetic and seismic modeling for CO_2 detection and monitoring in a saline aquifer: Journal of Petroleum Science and Engineering, **100**, 162–172, doi: 10.1016/j.petrol.2012.03.018.

Carcione, J. M., and S. Picotti, 2006, P-wave seismic attenuation by slow-wave diffusion. Effects of inhomogeneous rock properties: Geophysics, **71**, no. 3, O1–O8, doi: 10.1190/1.2194512.

Ding, P. B., B. R. Di, D. Wang, J. X. Wei, and L. B. Zeng, 2018, P- and S-wave velocity and anisotropy in saturated rocks with aligned cracks: Wave Motion, **81**, 1–14, doi: 10.1016/j.wavemoti.2018.05.001.

Dutta, N. C., and H. Odé, 1979, Attenuation and dispersion of compressional waves in fluid-filled porous rocks with partial gas saturation (White model) — Part 1: Biot Theory: Geophysics, **44**, 1777–1788, doi: 10.1190/1.1440938.

Dutta, N. C., and A. J. Seriff, 1979, On White's model of attenuation in rocks with partial gas saturation: Geophysics, **44**, 1806–1812, doi: 10.1190/1.1440940.

Dvorkin, J., and G. Mavko, 2006, Modeling attenuation in reservoir and nonreservoir rock: The Leading Edge, **25**, 194–197, doi: 10.1190/1.2172312.

Dvorkin, J., G. Mavko, and A. Nur, 1995, Squirt flow in fully saturated rocks: Geophysics, **60**, 97–107, doi: 10.1190/1.1443767.

Dvorkin, J., R. Nolen-Hoeksema, and A. Nur, 1994, The Squirt-flow mechanism: Macroscopic description: Geophysics, **59**, 428–438, doi: 10.1190/1.1443605.

Guo, J., G. J. Rubino, N. D. Barbosa, S. Glubokovskikh, and B. Gurevich, 2018a, Seismic dispersion and attenuation in saturated porous rocks with aligned fractures of finite thickness: Theory and numerical simulations — Part 1: P-wave perpendicular to the fracture plane: Geophysics, **83**, no. 1, WA49–WA62, doi: 10.1190/geo2017-0065.1.

Guo, J., G. J. Rubino, N. D. Barbosa, S. Glubokovskikh, and B. Gurevich, 2018b, Seismic dispersion and attenuation in saturated porous rocks with aligned fractures of finite thickness: Theory and numerical simulations — Part 2: Frequency-dependent anisotropy: Geophysics, **83**, no. 1, WA63–WA71, doi: 10.1190/geo2017-0066.1.

Guo, M. Q., J. Ba, R. P. Ma, T. Chen, L. Zhang, M. Pang, and J. Xie, 2018c, P-wave velocity dispersion and attenuation in fluid-saturated tight sandstones: Characteristics analysis based on a double double-porosity structure model description (in Chinese): Chinese Journal of Geophysics, **61**, 1053–1068.

Guo, M. Q., and L. Y. Fu, 2006, Stress associated coda attenuation from ultrasonic waveform measurements: Geophysical Research Letters, **34**, L09307.

Guo, M. Q., L. Y. Fu, and J. Ba, 2009, Comparison of stress-associated coda attenuation and intrinsic attenuation from ultrasonic measurements: Geophysical Journal International, **178**, 447–456, doi: 10.1111/j.1365-246X.2009.04159.x.

Guo, Y. Q., H. D. Ma, J. Ba, Y. Has, and C. Long, 2015, Impact of data distribution on fluid sensitivity analysis: A quantitative investigation: Journal of Applied Geophysics, **119**, 1–15, doi: 10.1016/j.jappgeo.2015.05.003.

Gurevich, B., M. Brajanovski, R. J. Galvin, T. M. Müller, and J. T. Stewart, 2009, P-wave dispersion and attenuation in fractured and porous reservoirs — Poroelasticity approach: Geophysical Prospecting, **57**, 225–237, doi: 10.1111/j.1365-2478.2009.00785.x.

Hill, R., 1952, The elastic behaviour of a crystalline aggregate: Proceedings of the Physical Society, **65**, 349–354, doi: 10.1088/0370-1298/65/5/307.

Hu, C., N. Tu, and W. Lu, 2013, Seismic attenuation estimation using an improved frequency-shift method: IEEE Geoscience and Remote Sensing Letters, **10**, 1026–1030, doi: 10.1109/LGRS.2012.2227933.

Johnson, D. L., 2001, Theory of frequency dependent acoustics in patchy-saturated porous media: Journal of the Acoustical Society of America, **110**, 682–694, doi: 10.1121/1.1381021.

Kong, L., B. Gurevich, T. M. Müller, Y. Wang, and H. Yang, 2013, Effect of fracture fill on seismic attenuation and dispersion in fractured porous rocks: Geophysical Journal International, **195**, 1679–1688, doi: 10.1093/gji/ggt354.

Kong, L., B. Gurevich, Y. Zhang, and Y. Wang, 2017, Effect of fracture fill on frequency-dependent anisotropy of fractured porous rocks: Geophysical Prospecting, **65**, 1649–1661, doi: 10.1111/1365-2478.12505.

Kumar, M., and D. Han, 2005, Pore shape effect on elastic properties of carbonate rocks: 75th Annual International Meeting, SEG, Expanded Abstracts, 1477–1480, doi: 10.1190/1.2147969.

Li, F., H. Zhou, N. Jiang, J. Bi, and K. J. Marfurt, 2015, Q estimation from reflection seismic data for hydrocarbon detection using a modified frequency shift method: Journal of Geophysics and Engineering, **12**, 577–586, doi: 10.1088/1742-2132/12/4/577.

Liu, L. F., and Z. D. Sun, 2009, Application of seismic wave absorption and attenuation technology in predicting fracture-vug carbonate reservoir: Oil Geophysical Prospecting, **44**, 121–124.

Mavko, G., T. Mukerji, and J. Dvorkin, 2009, The rock physics handbook: Tools for seismic analysis of porous media: Cambridge University Press.
Mikhaltsevitch, V., M. Lebedev, and B. Gurevich, 2016, Laboratory measurements of the effect of fluid saturation on elastic properties of carbonates at seismic frequencies: Geophysical Prospecting, **64**, 799–809, doi: 10.1111/1365-2478.12404.
Mousavi, M. A., M. Prodanovic, and D. Jacobi, 2012, New classification of carbonate rocks for process-based pore-scale modeling: SPE Journal, **18**, 243–263, doi: 10.2118/163073-PA.
Picotti, S., and J. M. Carcione, 2006, Estimating seismic attenuation (Q) in the presence of random noise: Journal of Seismic Exploration, **15**, 165–181.
Picotti, S., J. M. Carcione, and J. Ba, 2018, Rock-physics templates for seismic Q: Geophysics, **84**, no. 1, MR13–MR23, doi: 10.1190/geo2018-0017.1.
Pride, S. R., and J. G. Berryman, 2003a, Linear dynamics of double porosity and dual-permeability materials. 1: Governing equations and acoustic attenuation: Physical Review E, **68**, 036603, doi: 10.1103/PhysRevE.68.036603.
Pride, S. R., and J. G. Berryman, 2003b, Linear dynamics of double porosity and dual-permeability materials. 2: Fluid transport equations: Physical Review E, **68**, 036604, doi: 10.1103/PhysRevE.68.036604.
Pride, S. R., J. G. Berryman, and J. M. Harris, 2004, Seismic attenuation due to wave induced flow: Journal of Geophysical Research, **109**, B01201, doi: 10.1029/2003JB002639.
Qin, X. L., X. Y. Li, Z. N. Cao, and Y. Liu, 2018b, The effect of water saturation on P-wave dispersion in fractured porous medium with two immiscible fluids: Journal of Geophysics and Engineering, **15**, 2556–2565, doi: 10.1088/1742-2140/aadb76.
Qin, X. L., X. Y. Li, S. Q. Chen, and Y. Liu, 2018a, The modeling and analysis of frequency-dependent characteristics in fractured porous media: Journal of Geophysics and Engineering, **15**, 1943–1952, doi: 10.1088/1742-2140/aac130.
Quan, Y. L., and J. M. Harris, 1997, Seismic attenuation tomography using the frequency shift method: Geophysics, **62**, 895–905, doi: 10.1190/1.1444197.
Quintal, B., 2012, Frequency-dependent attenuation as a potential indicator of oil saturation: Journal of Applied Geophysics, **82**, 119–128, doi: 10.1016/j.jappgeo.2012.03.001.
Rasolofosaon, P. N., and B. E. Zinszner, 2007, The unreasonable success of Gassmann's theory revisited: Journal of Seismic Exploration, **16**, 281–301.
Reuss, A., 1929, Calculation of the flow limits of mixed crystals on the basis of the plasticity of monocrystals: Zeitschrift fur Angewandte Mathematik und Mechanik, **9**, 49–58.
Sayers, C. M., 2008, The elastic properties of carbonates: The Leading Edge, **27**, 1020–1024, doi: 10.1190/1.2967555.
Spencer, J. W., and J. Shine, 2016, Seismic wave attenuation and modulus dispersion in sandstones: Geophysics, **81**, no. 3, D211–D231, doi: 10.1190/geo2015-0342.1.
Sun, S. Z., H. Wang, Z. Liu, Y. Li, X. Zhou, and Z. Wang, 2012, The theory and application of DEM-Gassmann rock physics model for complex carbonate reservoirs: The Leading Edge, **31**, 152–158, doi: 10.1190/1.3686912.
Tillotson, P., M. Chapman, J. Sothcott, A. I. Best, and X.-Y. Li, 2014, Pore fluid viscosity effects on P- and S-wave anisotropy in synthetic silica-cemented sandstone with aligned fractures: Geophysical Prospecting, **62**, 1238–1252, doi: 10.1111/1365-2478.12194.
Toksöz, M. N., D. H. Johnston, and A. Timur, 1979, Attenuation of seismic waves in dry and saturated rocks — 1: Laboratory measurements: Geophysics, **44**, 681–690, doi: 10.1190/1.1440969.
Tu, N., and W. Lu, 2009, An improved peak-frequency-shift method for Q estimation: International Geophysical Conference and Exposition.
Voigt, W., 1910, Lehrbuch der Kirstallphysik: Teubner.
Wang, D., S. L. Qu, P. B. Ding, and Q. Zhao, 2017, Analysis of dynamic fracture compliance based on poroelastic theory — Part 1: Model formulation and analytical expressions: Pure and Applied Geophysics, **174**, 2103–2120, doi: 10.1007/s00024-017-1511-4.
Wang, D., L. Wang, and P. B. Ding, 2016, The effects of fracture permeability on acoustic wave propagation in the porous media: A microscopic perspective: Ultrasonics, **70**, 266–274, doi: 10.1016/j.ultras.2016.05.013.
White, J. E., 1975, Computed seismic speeds and attenuation in rocks with partial gas saturation: Geophysics, **40**, 224–232, doi: 10.1190/1.1440520.
Xu, S. Y., and M. A. Payne, 2009, Modeling elastic properties in carbonate rocks: The Leading Edge, **28**, 66–74, doi: 10.1190/1.3064148.
Zeng, Q. C., M. Q. Guo, R. Jiang, J. Ba, H. Ma, and J. Liu, 2017, Fluid sensitivity of rock physics parameters in reservoirs: Quantitative analysis: Journal of Seismic Exploration, **26**, 125–140.
Zhang, C. J., and T. J. Ulrych, 2002, Estimation of quality factors from CMP records: Geophysics, **67**, 1542–1547, doi: 10.1190/1.1512799.
Zhang, L., J. Ba, W. Yin, W. Sun, and J.-Y. Tang, 2017, Seismic wave propagation equations of conglomerate reservoirs: A triple-porosity structure model (in Chinese): Chinese Journal of Geophysics, **60**, 1073–1087.
Zhang, S. X., C. C. Zou, and C. Peng, 2018, Numerical simulation study of anisotropic velocities in fractured-vuggy carbonate reservoirs: Journal of Geophysics and Engineering, **15**, 1851–1863, doi: 10.1088/1742-2140/aabd3f.